Tuning of magnetic properties of aluminium-doped strontium hexaferrite powders

Xiao-Mei Ma(马小梅), Jie Liu(刘杰), Sheng-Zhi Zhu(朱生志), and Hui-Gang Shi(史慧刚)†

Key Laboratory for Magnetism and Magnetic Materials of the Ministry of Education, Lanzhou University, Lanzhou 730000, China

(Received 22 June 2016; revised manuscript received 18 August 2016; published online 25 October 2016)

M-type Al-doped strontium ferrite powders ($SrAl_xFe_{2n-x}O_{19}$, $n = 5.9$) with nominal Al content of $x = 0$–2.0 are prepared by traditional ceramic technology. The phase identification of the powders, performed using x-ray diffraction, shows the presence of purity hexaferrite structure and absence of any secondary phase. The lattice parameters decrease with increasing x. The average grain size of the powders is about 300 nm–400 nm at Al^{3+} ion content $x = 0$–2.0. The room-temperature hysteresis loops of the powders, measured by using vibrating sample magnetometer, show that the specific saturation magnetization (σ_s) value continuously decreases while the coercivity (H_c) value increases with increasing x, and H_c reaches to 9759 Oe (1 Oe = 79.5775 A/m) at $x = 2.0$. According to the law of approach saturation, H_c value increases with increasing Al^{3+} ion content, which is attributed to the saturation magnetization (M_s) decreasing more rapidly than the magnetic anisotropy constant (K_1) obtained by numerical fitting of the hysteresis loops. The distribution of Al^{3+} ions in the hexaferrite structure of $SrAl_xFe_{2n-x}O_{19}$ is investigated by using ^{57}Co Mössbauer spectroscopy. The effect of Al^{3+} doping on static magnetic properties contributes to the improvement of magnetic anisotropy field.

Keywords: Al-doped, strontium ferrite powders, high coercivity

PACS: 61.46.–w, 75.75.–c **DOI:** 10.1088/1674-1056/25/12/126102

1. Introduction

M-type hexagonal ferrite ($MFe_{12}O_{19}$, M is divalent cation, such as Ba^{2+}, Sr^{2+}, and so on), is one of the most used hard magnetic materials with applications such as permanent magnets, magnetic recording media due to their low cost, good chemical stabilities, high coercivities, high saturation magnetizations, and large magnetocrystalline anisotropies.[1–5] Recently, the barium ferrite was widely used as magnetic recording media, microwave devices, and electromagnetic wave absorbers.[3,6,7] Furthermore, various methods of fabricating the M-type hexaferrite have been developed including sol-gel method,[8,9] co-precipitation,[10,11] ceramic method,[12,13] and hydrothermal method,[14] citrate auto-combustion,[15] and glycin–nitrate method.[16]

In order to change physical properties, substituting some cations into SrM structure is an effective method to cope with the different applications. A lot of work has been done to modify the magnetic parameters of SrM by substituting Fe^{3+} with other cations, such as Al^{3+}, Cr^{3+}, Ga^{3+}, and so on.[17–19] The magnetic properties of substituted hexaferrites directly depend on the electronic configuration of the dopant cations as well as their preference to occupy the different Fe sub-lattices of the magnetoplumbite structure.[20] In particular, as is well known, Al-substituted SrM has very large coercivity.[17,21,22] Furthermore, it is important to understand the mechanism for increasing the coercivity by Al^{3+} doping.

SrM with hexagonal structure and molecular formula $SrFe_{12}O_{19}$ has a magnetoplumbite (M) structure which was determined by Adelsklod.[23,24] The crystal structure can be separated into two blocks, one block is R Block ($Fe_6O_8^{2+}$) and another one is S block ($BaFe_6O_{11}^{2-}$), R^*S^* block can be obtained by rotating the corresponding block 180° around the hexagonal c axis, so the chemical composition of the unit cell is $Sr_2Fe_{24}O_{38}$. The 24 Fe^{3+} ions of the unit cell are among five different crystal sites, i.e., three octahedral sites (12k, 4f_2, and 2a), one tetrahedron site (4f_1) and one trigonal bipyramidal site (2b).[25] The 16 Fe^{3+} ions with upward spins are located at 2a, 2b, and 12k, whereas the remaining 8 Fe^{3+} ions are located at 4f_1 and 4f_2 with downward spins, which result in a net magnetic moment of 40 μ_B per unit cell.[26] It has large magnetocrystalline anisotropy by the strong exchange interaction among the Fe^{3+} ions. Therefore the substitution for Fe ions could be an effective way to modify the magnetic properties.

In this study, we prepare Al^{3+}-doped SrM by traditional ceramic technology, and the coercivity reaches to 9759 Oe at $x = 2.0$. We attempt to understand in detail the reasons and the mechanism of enhancing the coercivity and magnetic structure formation of $SrAl_xFe_{2n-x}O_{19}$ as a function of the substituted amounts of dopants in a range ($0 \leq x \leq 2.0$).

2. Experiment

$SrAl_xFe_{2n-x}O_{19}$ ($n = 5.9$ $x = 0$–2.0) samples were prepared via ball milling appropriate mixtures of $SrCO_3$, Fe_2O_3 and Al_2O_3 powders. The amount of each compound was de-

†Corresponding author. E-mail: shihuig@lzu.edu.cn

© 2016 Chinese Physical Society and IOP Publishing Ltd

termined for each particular stoichiometry of $SrAl_xFe_{2n-x}O_{19}$ and then mixed in a ball milling cylinder. The mechanical alloying was carried out in a traditional ball mill for 4 h and the volume ratio of alcohol to powders was about 1.5:1. After milling, the powders were placed into cylindrical pellets. Calcination was then carried out for 2 h in air at 1200 °C.

The phase composition and crystal structure were analyzed by using Bruker diffractometer with Cu K_α x-ray diffraction measurement ($\lambda = 1.5406$ Å); scanning electron microscopy was employed to analyze the morphologies and microstructures of the samples. Magnetic properties could be obtained by analyzing the data of the vibrating sample magnetometer and the Mössbauer spectroscopy. The Mössbauer spectrum at room temperature was recorded using a Mössbauer spectrometer operating in constant acceleration mode (triangular wave) in transmission geometry. The source employed was ^{57}Co in Rh matrix of strength 50 mCi. The velocity was scaled by using an enriched a-Fe metal foil under an effective nuclear hyperfine field ($H_{\rm eff}$) of 331 kOe at room temperature.

3. Result and discussion

Figure 1 shows the typical x-ray diffraction (XRD) patterns of the precursor powders without and with various Al concentrations ($x = 0$–2.0) annealed for 2 h at 1200 °C. All the XRD patterns are similar, and consist of a set of strong diffraction profiles, which are similar to those of the $SrFe_{12}O_{19}$ (ICCD card No. 79-1411). There is no impurity phase (no additional minor peaks can be observed), thus confirming the formation of pure and well-crystallized phase. It is found that the peak positions systematically shift towards the high values with increasing doping concentration, which shows that there appears to be some change in crystal structure as x increases.

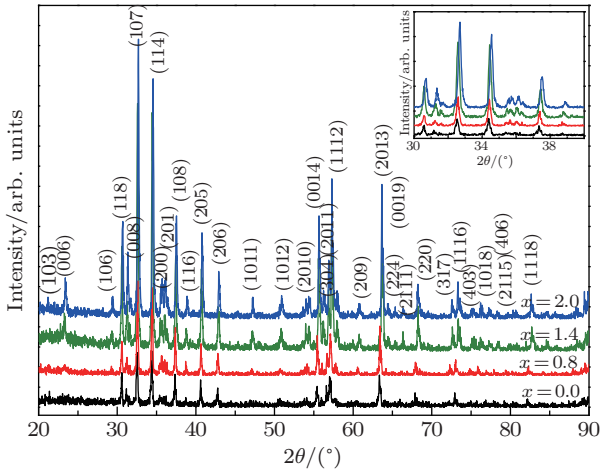


Fig. 1. (color online) XRD patterns of $SrAl_xFe_{2n-x}O_{19}$ at $T = 1200$ °C.

The lattice parameters a and c of $SrAl_xFe_{2n-x}O_{19}$ ($n = 5.9$, $x = 0$–2.0) are calculated according to the following formula:

$$\frac{1}{d^2_{(hkl)}} = \frac{4}{3} \times \frac{h^2 + hk + k^2}{a^2} + \frac{l^2}{c^2}, \tag{1}$$

where h, k, and l are Miller indices and d is the interplanar spacing as determined by the Bragg formula, $2d \sin\theta = n\lambda$. The unit cell volume is calculated by using the lattice parameters a and c from the following formula:[27,28]

$$V_{\rm cell} = \frac{\sqrt{3}}{2} a^2 c. \tag{2}$$

The x-ray density, ρ_x, of the material is calculated according to the following relation:

$$\rho_x = \frac{2M}{N_{\rm a} V_{\rm cell}}, \tag{3}$$

where M represents the molar mass of the sample and $N_{\rm a}$ is the Avogadro's number.

The changes of structural parameters, density and volume with composition are given in Table 1. It can be observed that the values of lattice parameters a and c decrease with x increasing from 5.89 Å to 5.84 Å and from 23.11 Å to 22.89 Å, respectively. This decrease becomes slow with composition rising up to $x = 1.4$ and then decreases dramatically for $x = 2.0$. As a result, the volume also decreases, which is attributed to the radius of Al^{3+} (0.535 Å) being smaller than that of Fe^{3+} (0.645 Å).[29] Furthermore, the density of samples decreases with increasing x.

Table 1. Values of crystal lattice a and c, the unit-cell volume and the density for $SrAl_xFe_{2n-x}O_{19}$.

Composition (x)	a/Å	c/Å	$V/10^{-22}$ cm^3	ρ_x/(g/cm^3)
0	5.89	23.11	6.94	5.03
0.8	5.88	23.05	6.90	4.95
1.4	5.87	23.00	6.86	4.89
2.0	5.84	22.89	6.76	4.88

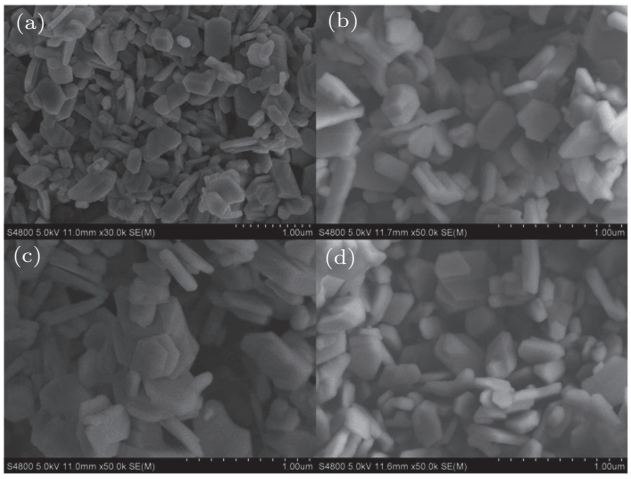


Fig. 2. Scanning electron micrographs of $SrAl_xFe_{2n-x}O_{19}$ magnetic powder particles with (a) $x = 0$, (b) $x = 0.8$, (c) $x = 1.4$, (d) $x = 2.0$.

Particle size and morphology are studied by SEM as shown in Figs. 2(a)–2(d). It is noteworthy that there is nearly no change in grain size (300 nm to 400 nm) nor morphology in the range of Al^{3+} substitution from $x = 0$ to $x = 2.0$ at the same temperature. It could be considered that Al^{3+} substitution does not affect the particle size and morphology, but it makes great contributions to the lattice parameters and the magnetic properties. The influence on the magnetic properties will be discussed in detail later.

In the hexagonal structure of strontium ferrite, Fe^{3+} ions occupy five sites: $4f_1$, $2a$, $4f_2$, $12k$, and $2b$. The contributions of Fe^{3+} ions located on those sites to magnetic properties are different from each other. After Al^{3+} ions enter into the lattice and substitute for some Fe^{3+} ions, the magnetocrystalline anisotropy field is changed. From the Mössbauer spectra as shown in Fig. 3, the substitution sites can be investigated, and then the effect of substitution on anisotropy field can be revealed. The hyperfine parameters including hyperfine field, isomer shift, quadrupole splitting and Fe^{3+} occupation area ratio are shown in Figs. 4–7. It can be observed in Fig. 4 that the isomer shifts of octahedral sites ($12k$, $4f_2$, and $2a$) are greater than those of tetrahedron sites, because the electron density of Fe^{3+} ions at octahedral sites is smaller than that at the octahedral sites. The isomer shift value in the range 0.24 mm/s–0.40 mm/s for five sites at $x = 0$–2.0 implies only the existence of high-spin Fe^{3+} cations.[30,31] In Fig. 5, the hyperfine fields of five sites are in the following sequence: $H_{hf}(2b) < H_{hf}(12k) < H_{hf}(4f_1) < H_{hf}(2a) < H_{hf}(4f_2)$, which is in agreement with the results reported by Evan *et al.*[32] The hyperfine field of each site decreases only slightly with increasing x, because the magnetic Fe^{3+} ions are replaced by non-magnetic Al^{3+} ions. The numbers of cations located at sites $12k$, , $4f_1$, $4f_2$, $2a$, and $2b$ are 6, 2, 2, 1, and 1 (per formula unit), and the theoretical areas of the sextets are 50, 16.7, 16.7,8.3, and 8.3, respectively. The sextet area is directly proportional to the number of Fe^{3+} ions in the corresponding sites.[30] In the present study, the corresponding values of relative areas for $x = 0$ are found to be 51, 11.2, 8.2, 22.4, and 7.2, which is caused by the overlapping of the spectral peaks. From Fig. 6, Al^{3+} mainly replaces Fe^{3+} on $2a$ and $4f_1$ sites for $x \leq 1.4$ as reported in Ref. [6]. For $x = 2.0$, the area of $12k$ sites has a sharp decline in the relative strength,which implies that Al^{3+} ions are more inclined to replace Fe^{3+} of $12k$ site than Fe^{3+} of $4f_1$ site. These results indicate that the substitution Al^{3+} ions occur mainly at $2a$, $4f_1$, and $12k$ sites, and Fe^{3+} of $2b$ site can hardly be substituted for $x \leq 2.0$. In Fig. 7, the quadrupole splitting value of $2b$ site is very large as compared with those of other sites, which is due to the strongly distorted environment around $2b$ site.[25,33] After Al^{3+} ions enter into the lattice and substitute for some Fe^{3+} ions, Mössbauer parameters of $SrAl_xFe_{2-x}O_{19}$ at room temperature are shown in Table 2.

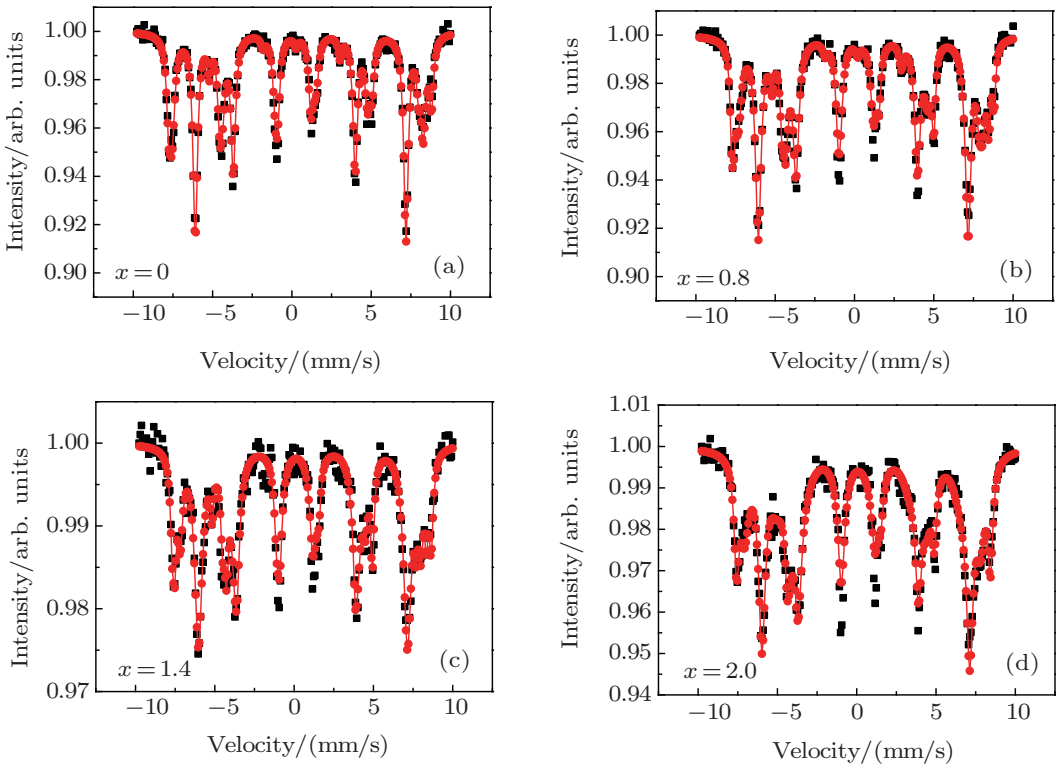


Fig. 3. (color online) The room temperature Mössbauer spectra of $SrAl_xFe_{2n-x}O_{19}$ with (a) $x = 0$, (b) $x = 0.8$, (c) $x = 1.4$, and (d) $x = 2.0$.

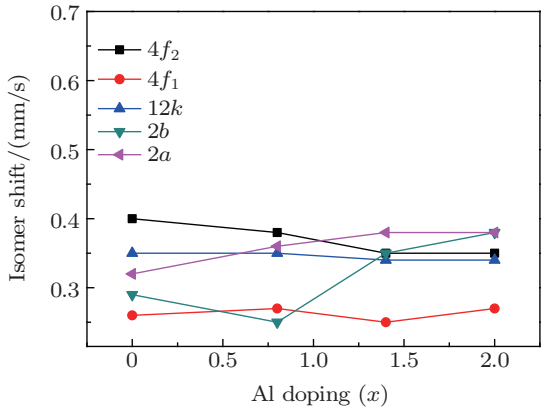


Fig. 4. (color online) Isomer shifts on five sites of $SrAl_xFe_{2n-x}O_{19}$.

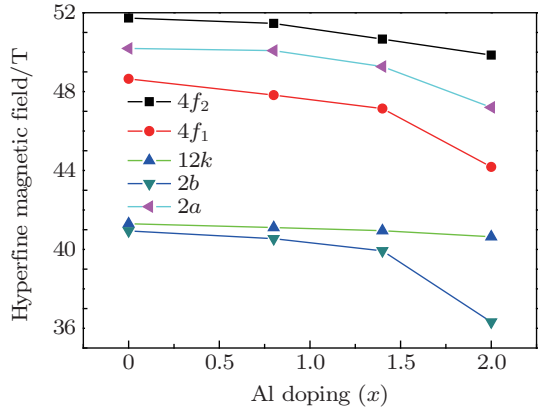


Fig. 5. (color online) Hyperfine fields on five sites of $SrAl_xFe_{2n-x}O_{19}$.

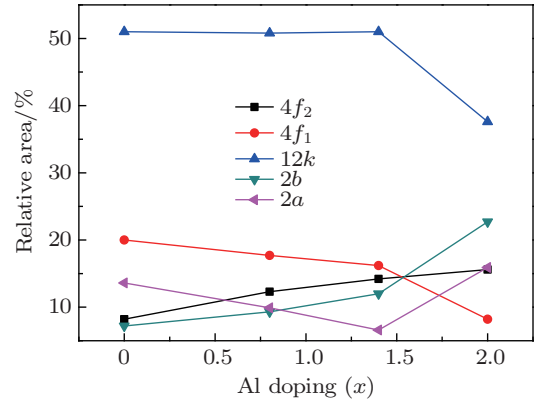


Fig. 6. (color online) Fe^{3+} ion occupation area ratio on five sites of $SrAl_xFe_{2n-x}O_{19}$.

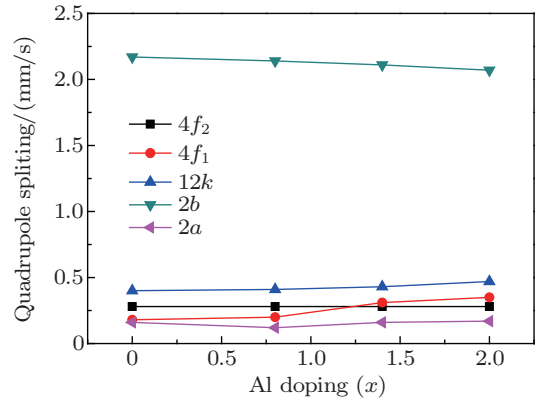


Fig. 7. (color online) Plots of quadrupole splitting versus Al doping amount on five sites of $SrAl_xFe_{2n-x}O_{19}$.

Table 2. Mössbauer parameters of $SrAl_xFe_{2n-x}O_{19}$ at room temperature.

	Site	H_{hf}/T	QS/(mm/s)	IS/(mm/s)	Spectral area/%
$x=0$	$4f_2$	51.73	0.28	0.40	8.2
	$4f_1$	48.65	0.18	0.26	20
	12k	41.30	0.40	0.35	51
	2b	40.94	2.17	0.29	7.2
	2a	50.19	0.16	0.32	13.6
$x=0.8$	$4f_2$	51.46	0.28	0.38	12.3
	$4f_1$	47.82	0.20	0.27	17.7
	12k	41.11	0.41	0.35	50.8
	2b	40.54	2.14	0.25	9.3
	2a	50.08	0.12	0.36	9.9
$x=1.4$	$4f_2$	50.66	0.28	0.35	14.2
	$4f_1$	47.14	0.31	0.25	16.2
	12k	40.95	0.43	0.34	51
	2b	39.93	2.11	0.33	12
	2a	49.27	0.16	0.38	6.6
$x=2.0$	$4f_2$	49.85	0.16	0.35	15.6
	$4f_1$	44.18	0.35	0.27	8.2
	12k	40.64	0.47	0.34	37.6
	2b	36.32	2.07	0.38	22.7
	2a	47.20	0.17	0.38	15.9

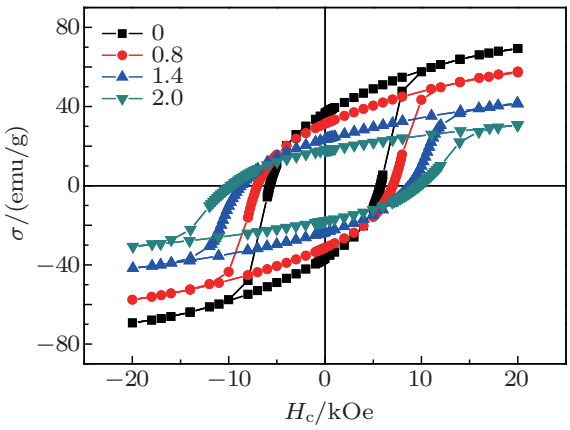


Fig. 8. (color online) M–H loops for $SrAl_xFe_{2n-x}O_{19}$ at 1200 °C.

The hysteresis loops of powder samples are measured at room temperature by using a vibrating sample magnetometer in Fig. 8. The H_c can be directly obtained from the loop. The magnetocrystalline anisotropy constant (K_1) and σ_s can be obtained by using the law of approach to saturation which is the sole static method to determine them for non-oriented polycrystalline materials. For the stage of approach to saturation in the hysteresis loop, the magnetization behavior can be described as[34–36]

$$M = M_s\left(1+\frac{A}{H}+\frac{B}{H^2}\right)+\chi H. \quad (4)$$

The A/H term is related to the existence of homogeneity in a microcrystal and is often ignored in the higher field case. The B/H^2 is related to the magnetic anisotropy constant.[33] The χ

is the high field susceptibility. For hexagonal ferrite, B can be defined as[36]

$$B = \frac{1}{15}H_{\rm A}^2 = \frac{4K_1^2}{15M_{\rm s}^2}. \quad (5)$$

The saturation magnetization $M_{\rm s}$ and magnetic anisotropy constant (K_1) can be obtained by fitting the hysteresis loop using Eqs. (4) and (5) as shown in Table 3. It is noticeable that the value of $M_{\rm s}$ decreases with increasing Al^{3+} doping, while the coercivity increases.

Table 3. The room temperature magnetic parameters of Al^{3+} substituted $SrAl_xFe_{2n-x}O_{19}$.

Composition x	$H_{\rm c}$/Oe	$M_{\rm s}$/(emu/cm^3)	$B/10^7$ Oe^2	$K_1/10^6$ (erg/cm^3)
0	5748.7	380.57	2.97	4.02
0.8	7031.9	297.16	3.97	3.98
1.4	8736.9	253.94	5.91	3.78
2.0	9759.2	183.20	8.64	3.30

The coercivity of M-type ferrite can be expressed as[37]

$$H_{\rm C} = 0.48(H_{\rm A} - H_{\rm D}). \quad (6)$$

Here, there are two kinds of anisotropies $H_{\rm A}$ and $H_{\rm D}$: $H_{\rm A}$ is magnetic anisotropy field and $H_{\rm D}$ is a shape-demagnetizing anisotropy field. Furthermore $H_{\rm D}$, which varies only with the shape of the particles, lies within a very small range (as the results show in Fig. 2). Therefore, the origin of the coercivity is derived from the magnetic anisotropy field $H_{\rm A}$, while $H_{\rm D}$ can be ignored. $H_{\rm A}$ can be given by[38]

$$H_{\rm A} = \frac{2K_1}{M_{\rm s}}. \quad (7)$$

In Fig. 9, it is obvious that the saturation magnetization $M_{\rm s}$ decreases more rapidly than the magnetic anisotropy constant (K_1) with the increase of Al^{3+} ion content, which can cause the magnetic anisotropy field to increase. As for the results of Mössbauer spectra, the reduction of saturation magnetization is attributed to the fact that the Al^{3+} ions preferentially occupy $2a$, $4f_1$, and $12k$ sites for $x \leq 2.0$, and a large number of Fe^{3+} on $12k$ sites, which are replaced by Al^{3+} contributed to the saturation magnetization, drastically decrease for $x = 2.0$. In addition, super-exchange interaction of Fe^{3+}–O^{2-}–Fe^{3+} is also among the factors that can influence the magnetic properties. Super-exchange interaction decreases with non-magnetic Al^{3+} replacing magnetic Fe^{3+} sites that can lead to the decrease of saturation magnetization. Furthermore, Xu *et al.*[39] found that the Fe^{3+} ions on $12k$ sites make a negative contribution to magnetocrystalline anisotropy constant, whereas Fe^{3+} ions on $2b$ sites result in a large positive contribution.[40] In this work, Al^{3+} ions mainly replace Fe^{3+} ions of $2a$, $4f_1$, and $12k$ sites and Fe^{3+} ions on $2b$ sites can hardly be substituted by Al^{3+} ions, as evidenced from the Mössbauer results for $x \leq 2.0$, which also causes the enhancement of magnetic anisotropy field.

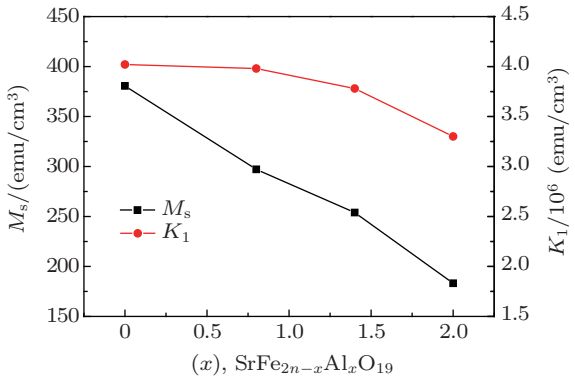


Fig. 9. (color online) Dependencies of saturation magnetization, $M_{\rm s}$, and magnetic anisotropy constant, K_1, on Al^{3+} ion substitution in $SrAl_xFe_{2n-x}O_{19}$.

4. Conclusions

A series of $SrAl_xFe_{2n-x}O_{19}$ powders ($n = 5.9$, $0 \leq x \leq 2.0$) are synthesized by conventional ceramic method. At low substitutions, Al^{3+} ions mainly occupy the $2a$, $4f_1$, and $12k$ sites of Fe^{3+}. At $x = 2.0$, the decrease of magnetizations is attributed to the fact that Fe^{3+} on $2b$ sites can hardly be substituted. The magnetic moment per unit cell, saturation magnetization and magnetic anisotropy constant decrease with increasing Al^{3+} substitution, while the coercivity increases. The enhancement of coercivity is caused by increasing magnetic anisotropy field, which is attributed to the fact that the saturation magnetization $(M_{\rm s})$ decreases more rapidly than the magnetic anisotropy constant (K_1) with the increase of Al^{3+} substitution.

Acknowledgment

The authors are thankful to Prof. Zheng Yang for discussion and suggestions and to Prof. Jianbo Wang for analyzing the Mössbauer spectra.

References

[1] Zou H, Li S H, Zhang L Q, Yan S H, Wu H G, Zhang S and Tian M 2011 *J. Magn. Magn. Mater.* **323** 1643
[2] Nie Y, Harward I, Balin K, Beaubien A and Celinski Z 2010 *J. Appl. Phys.* **107** 073903
[3] Dehlinger A S, LeBerre M, Canut B, Chatelon J P, Albertini D, Perrot S, Givord D and Rousseau J J 2010 *J. Magn. Magn. Mater.* **322** 3293
[4] Luo J H, Xu Y and Mao H K 2015 *J. Magn. Magn. Mater.* **381** 365
[5] Li T T, Li Y, Wu R N, Zhou H, Fang X C, Su S B, Xia A L, Jin C G and Liu X G 2015 *J. Magn. Magn. Mater.* **393** 325
[6] Qiu J X, Zhang Q G and Gu M Y 2005 *J. Appl. Phys.* **98** 103905
[7] Meng P Y, Xiong K, Ju K, Li S N and Xu G L 2015 *J. Magn. Magn. Mater.* **385** 407
[8] Sapoletova N A, Kushnir, S E, Li Y H, An S Y, Seo J W and Hur K H 2015 *J. Magn. Magn. Mater.* **389** 101
[9] Pawar R A, Desai S S, Tamboli Q Y, Shirsath S E and Paatange S M 2015 *J. Magn. Magn. Mater.* **378** 59
[10] Alam R S, Moradi M, Rostami M, Nikmannesh H, Moayedi R and Bai Y 2015 *J. Magn. Magn. Mater.* **381** 1
[11] Chin T S, Hsu S L and Deng M C 1993 *J. Magn. Magn. Mater.* **120** 64
[12] Lotgering F K 1974 *J. Phys & Chem. Solid* **35** 1633

[13] Van Uiteit L G 1957 *J. Appl. Phys.* **28** 317
[14] Pankov V V, Pernet M, Germi P and Mollard P 1993 *J. Magn. Magn. Mater.* **120** 69
[15] Shirtcliffea N J, Thompson S, O'Keefe E S, Appleton S and Perry C C 2007 *Mater. Res. Bull.* **42** 281
[16] Wang H Z, Yao B, Xu Y, He Q, Wen G H, Long S W, Fan J, Li G D, Shan L, Liu B, Jiang L N and Gao L L 2012 *J. Alloys Compd.* **537** 43
[17] Luo H, Rai B K, Mishra S H, Nguyen V V and Liu J P 2012 *J. Magn. Magn. Mater.* **324** 2602
[18] Kazina P E, Trusovb L A, Zaitsevb D D, Tretyakova Y D and Jansenc M 2008 *J. Magn. Magn. Mater.* **320** 1068
[19] Awawdeh M, Bsoul I and Mahmood S H 2014 *J. Alloys Compd.* **585** 465
[20] Ashiq M N, Iqbal M J and Gul I H 2011 *J. Magn. Magn. Mater.* **323** 259
[21] Choi D H, An S Y, Lee S W, Shim I B and Kim C S 2004 *Phys. Stat. Sol.* **241** 1736
[22] Chen D, Liu Y L, Li Y X, Yang K and Zhang H W 2013 *J. Magn. Magn. Mater.* **337–338** 65
[23] Adelskold V 1938 *Arkiv Kemi Miner. Geol.* **A12** 1
[24] Trukhanov A V, Turchenko V O, Bobrikov I A, Trukhanov S V, Kazakevich I S and Balagurov A M 2015 *J. Magn. Magn. Mater.* **393** 253
[25] Rai B K, Mishra S R, Nguyen V V and Liu J P 2013 *J. Alloys Compd.* **550** 198
[26] Tokunaga Y, Kaneko Y, Okuyama D, Ishiwata S, Arima T, Wakimoto S, Kakurai K, Taguchi Y and Tokura Y 2010 *Phys. Rev. lett.* **105** 2572
[27] Li W, Qiao X, Li M, Liu T and Peng H 2013 *Mater. Res. Bull.* **48** 4449
[28] Shams M H, Rozatian A S H, Yousefi M H, Valíček J and Šepelák V 2016 *J. Magn. Magn. Mater.* **399** 10
[29] Shannon R D, Prewitt C T and Crystallogr A 1969 *Sect. B: Struct. Sci.* **25** 925
[30] Katlakunta S, Meena S S, Srinath S, Bououdina M, Sandhya R and Praveena K 2015 *Mater. Res. Bull.* **63** 58
[31] Kelley P L, Kamzin A S, Romachevsky K E, Hue D T M, Chinh H D, Srikanth H and Phan M H 2015 *J. Alloys Compd.* **636** 323
[32] Evans B J, Grandjean F, Lilot A P, Vogel R H and Grard A 1987 *J. Magn. Magn. Mater.* **67** 123
[33] Araújo J H., Soares J M, Ginani M F, Machado F L A and Cunha J B M 2013 *J. Magn. Magn. Mater.* **343** 203
[34] Naranga S B, Singh C, Bai Y and Hudiara I S 2008 *Mater. Chem. Phys.* **111** 225
[35] Li Z W, Yang Z, Wei F L, Zhou X Z, Zhao J H and Morrish A H 2000 *Phys. Rev. B* **62** 6530
[36] Han M G, Ou Y, Chen W B and Deng L J 2009 *J. Alloys Compd.* **474** 18
[37] Haberey F and Velicescu M, *et al*. 1974 *Proc. Third European Conference on Hard Magnetic Materials*, September 17–19, 1974, Amsterdam, Netherlands, p. 70
[38] Ghasemi A and Morisako A 2008 *J. Alloys Compd.* **456** 485
[39] Xu Y, Yang G L, Chu D P and Ruzhai H 1990 *Phys. Stat. Sol. (b)* **157** 685
[40] Gossinger R 1981 *Phys. Stat. Sol. (a)* **66** 665